



# Monitoring opencast mine restorations using Unmanned Aerial System (UAS) imagery



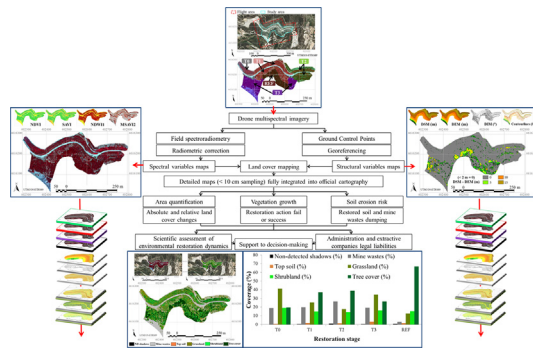
Joan-Cristian Padró <sup>a,\*</sup>, Vicenç Carabassa <sup>b</sup>, Jaume Balagué <sup>c</sup>, Lluís Brotons <sup>d</sup>, Josep M. Alcañiz <sup>e</sup>, Xavier Pons <sup>f</sup>

<sup>a</sup> Grumets Research Group, Departament de Geografia, Universitat Autònoma de Barcelona, Departament de Geografia Office B1092, Edifici B, Universitat Autònoma de Barcelona, 08193 Bellaterra, Catalonia, Spain  
<sup>b</sup> Centre de Recerca Ecològica i Aplicacions Forestals (CREAF), Edifici C, Campus UAB, 08193 Bellaterra, Catalonia, Spain  
<sup>c</sup> Centre Tecnològic Forestal de Catalunya (CTFC), Centre de Recerca Ecològica i Aplicacions Forestals (CREAF), Ctra Sant Llorenç km 2, 24280 Solsona, Catalonia, Spain  
<sup>d</sup> Centre Tecnològic Forestal de Catalunya (CTFC), Centre de Recerca Ecològica i Aplicacions Forestals (CREAF), Consejo Superior de Investigaciones Científicas (CSIC), Ctra Sant Llorenç km 2, 24280 Solsona, Catalonia, Spain  
<sup>e</sup> Universitat Autònoma de Barcelona, Centre de Recerca Ecològica i Aplicacions Forestals (CREAF), Edifici C, Universitat Autònoma de Barcelona, 08193 Bellaterra, Catalonia, Spain  
<sup>f</sup> Grumets Research Group, Departament de Geografia, Universitat Autònoma de Barcelona, Departament de Geografia Office B1094, Edifici B, Universitat Autònoma de Barcelona, 08193 Bellaterra, Catalonia, Spain

## HIGHLIGHTS

- Fast, repeatable and systematic monitoring at sub-decimeter spatial resolution
- R2 between drone imagery and field spectroradiometric measurements over 0.9
- Multispectral imagery allows monitoring mine wastes, restored soil and vegetation.
- A solution for easy detection of failing or successful restoration actions
- Affordable equipment and protocol for rigorous and non-conflictive mine monitoring

## GRAPHICAL ABSTRACT



## ARTICLE INFO

**Article history:**  
 Received 15 June 2018  
 Received in revised form 19 November 2018  
 Accepted 10 December 2018  
 Available online 13 December 2018

**Keywords:**  
 Mine restoration  
 Monitoring restoration

## ABSTRACT

Open-pit mine is still an unavoidable activity but can become unsustainable without the restoration of degraded sites. Monitoring the restoration after extractive activities is a legal requirement for mine companies and public administrations in many countries, involving financial provisions for environmental liabilities. The objective of this contribution is to present a rigorous, low-cost and easy-to-use application of Unmanned Aerial Systems (UAS) for supporting opencast mining and restoration monitoring, complementing the inspections with very high (<math><10\text{ cm}</math>) spatial resolution multispectral imagery, and improving any restoration documentation with detailed land cover maps. The potential of UAS as a tool to control restoration works is presented in a calcareous quarry that has undergone different post-mining restoration actions in the last 20 years, representing 4 reclaimed

**Abbreviations:** AGL, above ground level; ASPRS, American Society for Photogrammetry and Remote Sensing; DCSM, Digital Cast Shadow Model; DEM, Digital Elevation Model; DIM, Digital Illumination Model; DLS, Downwelling Light Sensor; DSM, Digital Surface Model; DTM, Digital Terrain Model; EVA, Ethylene-Vinyl Acetate; EXIF, Exchangeable Image File Format; FWHM, Full Width at Half Maximum; GCP, Ground Control Point; GIS, Geographical Information System; GNSS, Global Navigation Satellite System; GPS, Global Positioning System; GRE, green (spectral region); kNN, k-Nearest Neighbor; LDCM, Landsat Data Continuity Mission; lidar, Light Detection and Ranging; MSAVI, Modified Soil Adjusted Vegetation Index; NDVI, Normalized Difference Vegetation Index; NDWI, Normalized Difference Water Index; NIR, near-infrared (spectral region); RED, red (spectral region); REF, reference; REG, red edge (spectral region); ROI, Region Of Interest; RS, remote sensing; SAVI, Soil Adjusted Vegetation Index; TA, Training Area; TIN, Triangulated Irregular Network; TRA, Transit Area; UAS, Unmanned Aerial System; UAV, Unmanned Aerial Vehicle; VNIR, visible and near-infrared (spectral region); VA, Validation Area.

\* Corresponding author.

E-mail addresses: [JoanCristian.Padro@uab.cat](mailto:JoanCristian.Padro@uab.cat) (J.-C. Padró), [V.Carabassa@creaf.uab.cat](mailto:V.Carabassa@creaf.uab.cat) (V. Carabassa), [Jaume.Balague@ctfc.cat](mailto:Jaume.Balague@ctfc.cat) (J. Balagué), [Lluís.Brotons@ctfc.cat](mailto:Lluís.Brotons@ctfc.cat) (L. Brotons), [JoseMaria.Alcaniz@uab.cat](mailto:JoseMaria.Alcaniz@uab.cat) (J.M. Alcañiz), [Xavier.Pons@uab.cat](mailto:Xavier.Pons@uab.cat) (X. Pons).

Drone  
Unmanned Aerial System  
UAS  
UAV remote sensing  
Multispectral imagery

stages. We used a small (<2 kg) drone equipped with a multispectral sensor, along with field spectroradiometer measurements that were used to radiometrically correct the UAS sensor data. Imagery was processed with photogrammetric and Remote Sensing and Geographical Information Systems software, resulting in spectral information, vegetation and soil indices, structural information and land cover maps. Spectral data and land cover classification, which were validated through ground-truth plots, aided in the detection and quantification of mine waste dumping, bare soil and other land cover extension. Moreover, plant formations and vegetation development were evaluated, allowing a quantitative, but at the same time visual and intuitive comparison with the surrounding reference systems. The protocol resulting from this research constitutes a pipeline solution intended for the implementation by public administrations and private companies for precisely evaluating restoration dynamics in an expedient manner at a very affordable budget. Furthermore, the proposed solution prevents subjective interpretations by providing objective data, which integrate new technologies at the service of scientists, environmental managers and decision makers.

© 2018 The Authors. Published by Elsevier B.V. This is an open access article under the CC BY-NC-ND license (<http://creativecommons.org/licenses/by-nc-nd/4.0/>).

## 1. Introduction

Severe ecosystem changes are the result of opencast mining activities, which affect the soil, vegetation, fauna, hydrology and landforms (Drake et al., 2010). The restoration of degraded soils and human-disrupted landscapes involves a large number of priorities (Ockendon et al., 2018). Among them, post-mining restoration represents the specific challenge of creating ecological structures that become integrated into the surrounding environment, which starts from “point zero” (Hüttel and Weber, 2001). Mine wastes and rocky debris are common initial substrate conditions, being necessary artificially replacing soil (i.e. technosol) and introducing local vegetation by means of planting, sowing and encroaching the surrounding vegetation to drive the restoration process to pre-mining landscape conditions (Korjus et al., 2014). Ecological engineering scientists assume that after intensive opencast mining, the final soil conditions are usually extremely degraded thus leading the restoration process to either fail or simply not begin (Bradshaw, 1997). Consequently, the task of monitoring reclaimed areas becomes a fundamental feature in any restoration process, as it provides crucial information to environmental managers for those involved in assessing the success of adopted techniques (DITR, 2016). The objective of a restoration is to achieve a self-sustainable ecosystem at the overall affected landscape (Elmqvist et al., 2003). Restoration of opencast mines is regulated in most developed countries, and expected to be also in the remaining ones. For instance, in the European Union we can find different levels of legislation, the European (Directive 2006/21/EC), member states (e.g. Spanish RD975/2009, German Bundesberggesetz 1980) and regional governments (e.g. Catalan Law 12/1981), all of which require monitoring and periodically inspection of mine restorations. Moreover, extractive companies are required to provide a financial guarantee for environmental liabilities, which are blocked by the administration to assure that the companies comply with the regulations ensuring the proper restoration of the mined areas. Altogether, not only public administrations are interested in upholding legal measures for land restoration, also private companies want to recover the financial provision.

Environmental characterization, mapping and monitoring (Thenkabail, 2015) is one of the first and most productive applications of remote sensing (RS). The scientific use of environmental remote sensing data has been evolving since the 1970s, when the first Landsat satellite was put into orbit. The Landsat Data Continuity Mission (LDCM) (NASA, 2018), which has been the standard-bearer of Earth resources and environmental monitoring from space, uses sensors in the solar [0.450  $\mu\text{m}$  to 2.500  $\mu\text{m}$ ] and thermal [8  $\mu\text{m}$  to 13  $\mu\text{m}$ ] regions of the electromagnetic spectrum. The recent Sentinel-2 mission (ESA, 2015), which is represented by the Sentinel-2A and B platforms, is improving the spatial, spectral and temporal resolution of the free available satellite acquisitions. The joint synergy of those Earth observation programs is currently coordinated in the Global Earth Observation System of Systems (GEOSS). However, the Sentinel-2 spatial resolution (up

to 10 m) is not detailed enough to monitor slight land cover changes in relatively small areas of interest, such as some opencast mine restorations, despite some studies have been done combining Landsat imagery and in-situ monitoring (e.g. Bonifazi et al., 2003). Alternatively, a much more detailed spatial and spectral resolution can be reached with airborne optical sensors, such as the Airborne Hyperspectral Scanner, which features 80 bands from visible to thermal regions, or the Compact Airborne Spectrographic Imager 1500, which features 288 bands between 0.35  $\mu\text{m}$  and 1050  $\mu\text{m}$ , allowing sub-metric pixels at a standard flight height of 3000 m above ground level (AGL). Light Detection and Ranging (lidar) sensors can be effectively used to reconstruct the vegetation structure (Listopad et al., 2015) and classify land cover surfaces in combination with optical imagery, but the cost of taking off a plane with this expensive payload solely for the purpose of monitoring a mine restoration is ultimately not cost-effective. Moreover, satellite and airborne optical imagery is often constrained by cloud cover conditions. On the other hand, such conditions do not pose a problem for lidar or optical sensors onboard Unmanned Aerial Systems (UAS or drones) when flying below the cloud cover thanks to their high sensitivity even when only diffuse irradiance exists. It is important to note that in such conditions, reflectance is much more Lambertian than under direct sunlight, and incoming diffuse irradiance can be measured in-situ at the time of the drone flight. A radiometric analysis of multispectral photogrammetric imagery acquired in different illumination conditions can be found in Markelin (2013). Then, the use of well-known remote sensing satellite and aerial techniques, which can be adapted to the imagery provided by multispectral optical sensors onboard low-weight drones (Sanders, 2017), can considerably facilitate the task of covering an area dimensioned to the platform, in that a much higher spatial resolution can be obtained with a low-cost revisit time and is not constricted to cloud cover. With all these advantages, such a solution can prove more suitable for the operative goal of acquiring RS data in monitoring mine exploitations and their restoration.

Although the regulation of <25 kg UAS may vary in each country, in most of them there are no major restrictions on their use in non-urban areas, such as in opencast mine undergoing restorations; nevertheless they comply with the regulations on flight height limitation and observing the security distance to airports, as recommended by the International Civil Aviation Organization (ICAO, 2011). Regulations aside, the proliferation of low-cost and low-weight UAS as data acquisition tools is rapidly promoting the transference of knowledge from the research sphere to the productive economy, and vice versa. Many studies make use of multispectral optical sensors onboard low-weight (<25 kg) drones and apply remote sensing techniques for wide-ranging applications, such as the 3D reconstruction of cultural heritage sites (Eisenbeiss and Zhang, 2006), identifying and evaluating climate-related diseases (Yoo et al., 2017), precision agriculture (Díaz-Varela et al., 2015), topography (Lucieer et al., 2014) or wildfire severity (Pla et al., 2017). Altogether these studies focus intensely on space and time due to the nature of the UAS platforms (fixed-wing or rotary-wing), which can

acquire images with ultra-high spatial resolution, usually from 1 cm to 10 cm depending on the flight height and the sensor instantaneous field of view. The extraction activities sector is also very interested in UAS remote sensing applications. When dealing with opencast mining cases, we find that extractive companies are interested in 3D quantification of mineral resource volumes (Xu et al., 2015) or the geomorphic characterization (Chen et al., 2015), while the environmental community is mainly focused on monitoring water and soil pollution (Capolupo et al., 2015). To the best known of the authors, there are no applications of UAS imagery specifically designed for the “standardized” monitoring of opencast mine restorations, a legal issue pointed out in much of the environmental legislations and that involves public administrations, companies, technicians and wastes time and economic resources (Minerals Council of Australia, 2015). The interaction of these actors is susceptible to involve subjective appreciations of a given restoration, so we propose a workflow for acquiring highly detailed imagery to produce thematic maps and complement on-field evaluation with objective cartographic evidences.

The current geometric theoretical basis of UAS remote sensing finds its roots in digital photogrammetry and computer vision background (Hartley and Zisserman, 2003; Granshaw and Fraser, 2015). Generally, multiple overlapped photographs are acquired and a bundle block adjustment is performed using aero-triangulation techniques. Homologous points between adjacent photographs are automatically detected by using computer vision techniques, which are further used as tie points to fit the whole model, by forming a mosaic of the photographs and reconstructing the surface with the stereo photogrammetric information. There are two georeferencing methods mostly used in UAS imagery: direct georeferencing and indirect georeferencing. Direct georeferencing is based on integrated navigation systems, which uses Global Navigation Satellite Systems (GNSS), e.g. GPS receiver as well as Inertial Measurement Unit (IMU) information to locate the camera perspective center and estimate its orientation parameters at the acquisition time (Skaloud et al., 2014; Rehak and Skaloud, 2017). In fact, the quality and accuracy of the onboard GNSS and IMU are key factors for proper direct georeferencing. In contrast, indirect georeferencing of UAS imagery is based on Ground Control Points (GCP), scene locations with well-known coordinates (Rumpler et al., 2014). GCP are commonly measured with static post-processed GNSS methods and surrounded with a chessboard target that is visible in the UAS imagery. Comparatively, indirect georeferencing is more time-consuming than direct georeferencing, and the accuracy depends on the correct measurement of GCP positions, the technician's skill in locating the references in the imagery, and the number of GCPs, reaching pixel size accuracies (Turner et al., 2014). A recent comparison of four UAS georeferencing methods for environmental monitoring purposes can be found in Padró et al. (2019).

The radiometric theoretical basis of optical multispectral remote sensing in the visible and near infrared regions (VNIR), i.e. between 400 nm and 900 nm, is attained by measuring the spectral surface reflectance ( $\rho_\lambda$ ) in order to be comparable when imagery is acquired on different dates and/or by different sensors. Imagery is converted to  $\rho_\lambda$  at pixel level;  $\rho_\lambda$  is computed as the amount of spectral radiance ( $L_\lambda$ ) ( $\text{W} \cdot \text{m}^{-2} \cdot \text{sr}^{-1} \cdot \mu\text{m}^{-1}$ ) reflected by a surface located in a given pixel with respect to the total spectral irradiance ( $I_\lambda$ ) ( $\text{W} \cdot \text{m}^{-2} \cdot \mu\text{m}^{-1}$ ) received (Schaepmann-Strub et al., 2006). Satellite imagery is radiometrically corrected according to one of the different existing approaches (Kaufman and Sendra, 1988; Chavez, 1988; Pons et al., 2014; Vermote et al., 2016, as examples), and can be validated by using field spectroradiometric measurements as ground-truth (Padró et al., 2017). Moreover, as the incoming irradiance is difficult to approximate by modeling, it can be estimated empirically (Abdollahnejad et al., 2018), and as the UAS sensor is usually located in a very low AGL altitude (<120 m) the radiative transfer modeling has to be adapted or even substituted by other approaches (Aasen et al., 2015). A common approach for obtaining surface reflectance values from drone data

(Honkavaara et al., 2012; Iqbal et al., 2018) is the numerical fitting (usually an empirical line through reference targets) of UAS-acquired radiometry and field spectroscopy data. Additionally, there are consumer grade cameras with a Downwelling Light Sensor (DLS) that measures the total incoming irradiance at-sensor level, which stores this information in the EXIF file of each photograph and obtaining direct information to calculate at-sensor reflectance. Nevertheless, as Hakala et al. (2018) point out, the challenge in this method is that the upwards looking sensor has to be horizontally stabilized, which is typically not the case when using low-cost instruments.

The main objective of this research is to provide a new tool using UAS that generates detailed, objective, exhaustive and rigorous cartography of opencast mine restorations. Introducing of UAS for acquiring imagery as a source to obtain data and produce digital maps is expected to improve the diligence and objectiveness of inspections, and as such could reduce disagreements between public administrations and private companies. As a secondary goal, this research focuses on how, besides the intrinsic interest in the detailed imagery for visual inspections, UAS imagery can provide quantitative spatial information about restoration failures or success in terms of monitoring the area covered by vegetation, mine waste dumping or bare soil at different restoration stages.

## 2. Materials

### 2.1. Study area and restoration stages

The implementation for monitoring mine restorations using UAS was carried out in Catalonia, Spain, where 483 mine exploitations were documented in 2018 (GENCAT, 2018). We have developed the presented workflow on an active calcareous sandstone quarry located in central Catalonia (lat. 41° 41' 35"N lon. 1° 49' 43"E), with representative landforms corresponding to different stages of restoration, namely from old restorations carried out >20 years ago to recent plantations. By accessing the historic orthophotographs of 1957, 1984, 2000 and 2016 (ICGC, 2018a, 2018b), we can report that the land use of this area before the mining activity was dominated by vineyards (1957), which were abandoned and spontaneously forested by the encroachment of autochthonous species (1984). This is a good example of the transition forest theory (Mather and Needle, 1998) in Mediterranean environments (Padró and Badia, 2017; Poyatos et al., 2003). In this area, mining began in the mid-1980's, and hit its activity peak on the 2000's decade. The restoration stages considered were, from the present to the past, T<sub>0</sub> (0–5 years), T<sub>1</sub> (5–10 years), T<sub>2</sub> (10–15 years) and T<sub>3</sub> (15–20 years); additionally, a non-disturbed area was taken as reference (REF), and a Transit Area (TRA) was masked to avoid a bias in the quantification (Fig. 1).

The material extracted was calcareous sandstone, exploited through 10 m × 10 m banks. Bank-berm was the common landform model, resulting in steeped slopes. After a partial landform adaptation using mining debris, the surface was covered by new topsoil. The topsoil was a technosol, which was constructed using mine spoils and mineral sludge from the tailing process and was mixed with a small amount of previous topsoil stored for a long time. Organic amendments were added in order to increase soil fertility. Specifically, anaerobically digested sewage sludge was incorporated in a dose around 50 Mg/ha in order to increase soil organic matter, P and N contents, and improve soil aggregation. Revegetation measures consisted of sowing a mixture of herbaceous seeds (mainly grasses and leguminous) and planting local shrubs (mainly *Rosmarinus officinalis*) and trees (mainly *Pinus halepensis*), at a mean density of about 400 seedlings ha<sup>-1</sup>. Vegetation in restored areas presented different grades of development according to the age of sowing and planting activities, which range from adult trees and dense shrub cover in T<sub>3</sub>, to a dominant herbaceous cover in T<sub>0</sub>. The reference system (REF, undisturbed area) is a *Pinus halepensis* forest, with a dense shrub layer and a low herbaceous cover.

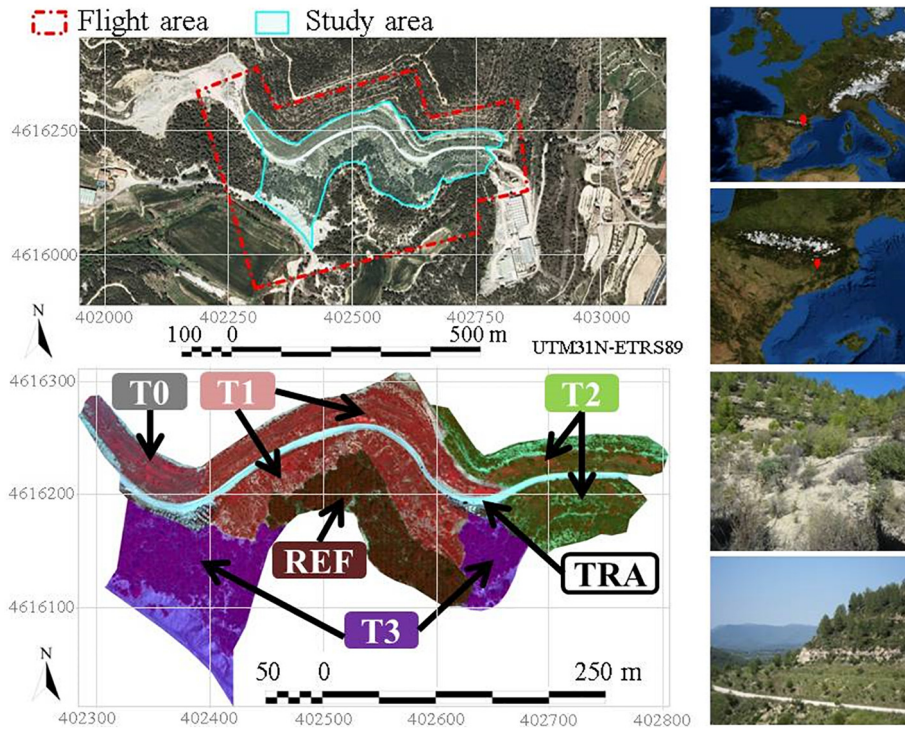


**Fig. 1.** Top left: Flight planned area and study area over the official local agency orthophotomap (ICGC, 2018a, 2018b). Bottom left: Restoration stages  $T_0$  (0–5 years),  $T_1$  (5–10 years),  $T_2$  (10–15 years) and  $T_3$  (15–20 years); non-altered area taken as reference (REF); Transit Area (TRA) masked to avoid bias in the quantification. Top right: Location maps. Bottom right: Restoration landscape.

The total dimension of the study area measured at 64,386 m<sup>2</sup>, which comprised of  $T_0$  4364 m<sup>2</sup>,  $T_1$  12,627 m<sup>2</sup>,  $T_2$  16,638 m<sup>2</sup>,  $T_3$  18,561 m<sup>2</sup>, REF 8206 m<sup>2</sup> and TRA 3990 m<sup>2</sup>. The planned flight (cf. Table S1 in the Supplementary materials) covered an additional area to assure the complete overlapping and preventing geometric distortions of the marginal photograms of the block. Previous flights were performed in mining activities to define a suitable flight altitude (90 m AGL) that balances the need for covering a typical opencast area and using a high spatial resolution product (<10 cm). These recommendations are in accordance with other experiences made in land cover classification of UAS imagery at different spatial resolutions (Ahmed et al., 2017).

It is worth noting that the season and the hour of the UAS data acquisition are crucial parameters to consider. After testing our method in all four seasons and at different hours of the day, we suggest that for acquiring imagery, in spring and summer are the best periods due to the leaf presence of deciduous vegetation, and during the hours of solar afternoon due to the high sun position, what minimizes shadows.

### 2.2. UAS sensor and platform

The optical sensor used on this study was a Parrot Sequoia (cf. Table S2 in the Supplementary materials), which is a multispectral sensor light enough to be embedded in <2 kg maximum take-off weight platforms. This sensor has four spectral bands (green (GRE), red (RED), red-edge (REG) and near infrared (NIR)), which are specifically disposed to improve the detection of vegetation and its features. The relative spectral response function (RSRF) is not provided by the manufacturer, and we assumed the Full Width Half Maximum (FWHM) provided in the specification sheet, by guessing the shape of the RSRF; other sensors providing detailed RSRF allow a more detailed integration (e.g. Padró et al., 2018). A detailed analysis of the Parrot Sequoia can be found in Fernández-Guisuraga et al. (2018). The Parrot Sequoia includes a DLS located at the top of the UAS, which registers the Sun total spectral irradiance at-sensor level and thus facilitates the automatic determination of the at-sensor reflectance. The performance of the DLS of the Parrot

Sequoia was tested with in-situ reference targets, and finally at-sensor reflectance was numerically fitted to surface reflectance spectroradiometric measurements. The platform used was a DJI Phantom III Advanced (DJI, 2018) quadcopter (cf. Table S3 in the Supplementary materials) due to its compatibility with Android and iOS systems, fitness to the proposed procedures, low-cost, easy manageability, reduced dimensions, and capacity of embedding the multispectral sensor that we used therein. The default optical sensor was substituted by the Parrot Sequoia, which was mounted on the gimbal (Fig. 2).

### 2.3. Field spectroradiometer

The in-situ ground-truth reflectance was measured with an OceanOptics USB2000+ portable field spectroradiometer (OceanOptics, 2006) (Table S4 in the Supplementary materials). USB2000+ widely covers the VNIR spectral range of the multispectral UAS sensor commonly used. The physical magnitude measured with the spectroradiometer is the spectral surface reflectance ( $\rho_\lambda$ ), as explained in Pons et al. (2015) and Meroni and Colombo (2009). In order to account for the variability of measurements, 100 readings were obtained for each measurement and the overall data was statistically analyzed (mean, median, standard deviation, etc.) to evaluate its coherence, whereby we synthesized 1 nm of spectral resolution signature of every given surface.

We used a set of 24 matt Ethylene-Vinyl Acetate (EVA) rubber (foam) artificial targets of different colors (violet, blue, sky blue, green, yellow, orange, pink, red, brown, grey and black) in order to have several spectral reflectance references. A lower number of targets can be used for an empirical line correction (e.g. using two, the targets should be dark and bright). When more than two targets are used, they should properly cover the reflectance range, but avoiding reflectance spectra intersections; if it is the case, a large number of spectra is recommended to be used (Richter and Schläpfer, 2016), and thus, we used a large number of targets. The EVA foam material presented a highly Lambertian behavior and was useful in different campaigns. We worked with two

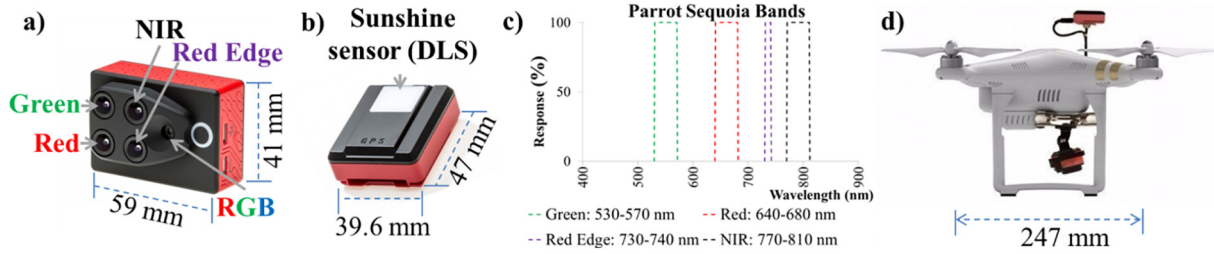


**Fig. 2.** UAS materials: (a) Parrot Sequoia multispectral sensor (b) Downwelling Light Sensor (DLS) (c) Nominal FWHM bandwidth (d) DJI Phantom III platform with the optical sensor equipment.

sizes of artificial targets, a group of 14 units of 50 cm × 50 cm × 2 cm (namely “EVA” in Fig. 3) and a group of 10 units of 40 cm × 60 cm × 0.2 cm (namely “foam” in Fig. 3). Those targets were big enough to be clearly seen in the UAS images (9 cm pixel size) with an equivalent surface of 30.9 pixels and 5.5 pixels × 5.5 pixels around the central pixel in the squared targets, and with an equivalent surface of 29.6 pixels and 4.4 pixels × 6.7 pixels in the rectangular targets. This always allowed one “pure” pixel (surrounded by 5 × 5 pixels) at the center in the squared targets, and, consequently, they were the preferred ones to relate the drone sensor values and the in-situ (spectroradiometer) values through fitting and testing. Rectangular targets were only used to complement the measurements since their pixels were not so symmetrically distributed around the central pixel.

Seven EVA targets were located in a shadow to experiment with diffuse irradiation conditions and support the de-shadowing process, while the remaining 17 targets were located under direct sunlight. To this end, the spectral signature of each target was integrated at the FWHM provided by the Parrot Sequoia manufacturer (Fig. 3).

**3. Methods**

**3.1. Use of the photogrammetric software**

We used Agisoft PhotoScan v.1.4.1 (Agisoft, 2018) photogrammetric software, which is widely used in current UAS projects (Kraaijenbrink et al., 2016). The software workflow initially locates the individual frames with the geotagged photocenters provided by the navigation GNSS, then uses automatic tie points to estimate more accurately the external coordinates (X,Y,Z) for every frame, and the orientation angles ( $\omega, \phi, \kappa$ ). The Parrot Sequoia is a frame multilens sensor that generates four non-registered raw images in DN values, but the photogrammetric software uses the internal geometric information stored in the EXIF file

of each image to register the multiple bands (Jhan et al., 2017). The orientation process was optimized by filtering out erroneous points and using GCPs that were obtained from the official reference points of this mining activity reported in the respective exploitation labor plan cartography, which were used for indirectly georeferencing the bundle block. The validation of the geometric accuracy was achieved using the cross-validation method and complying with the planimetry and altimetry standards of the American Society for Photogrammetry and Remote Sensing (ASPRS) for digital orthoimagery (ASPRS, 2014) (cf. Table S5 in the Supplementary materials). This process generated the bundle block adjustment with aero-triangulation, the individual images mosaicking and the photogrammetric construction of a dense point cloud with X, Y and Z coordinates. The 3D point cloud allowed the generation of a Triangulated Irregular Network (TIN), which was further rasterized in a Digital Surface Model (DSM), and finally outputting a georeferenced orthophotomosaic. Points classified as terrain were used to generate a Digital Elevation Model (DEM) and derive contour lines. DLS irradiance information stored in EXIF files was used to radiometrically correct each photogram, so as to obtain at-sensor reflectance values. The photogrammetric software output was composed by the orthophotomap, the DEM and the DSM, the elevation contour lines from the DEM, and the dense point cloud of each model.

**3.2. Use of the RS&GIS software**

We used MiraMon (Pons, 2016) RS&GIS software to radiometrically correct the at-sensor drone imagery, to generate the derived spectral and structural variables, to perform the digital classification to obtain land cover maps, and to integrate drone imagery with official mapping agencies cartography.

Shadow reduction is the first issue to be solved, processing separately those pixels irradiated with diffuse radiance (shadowed pixels)

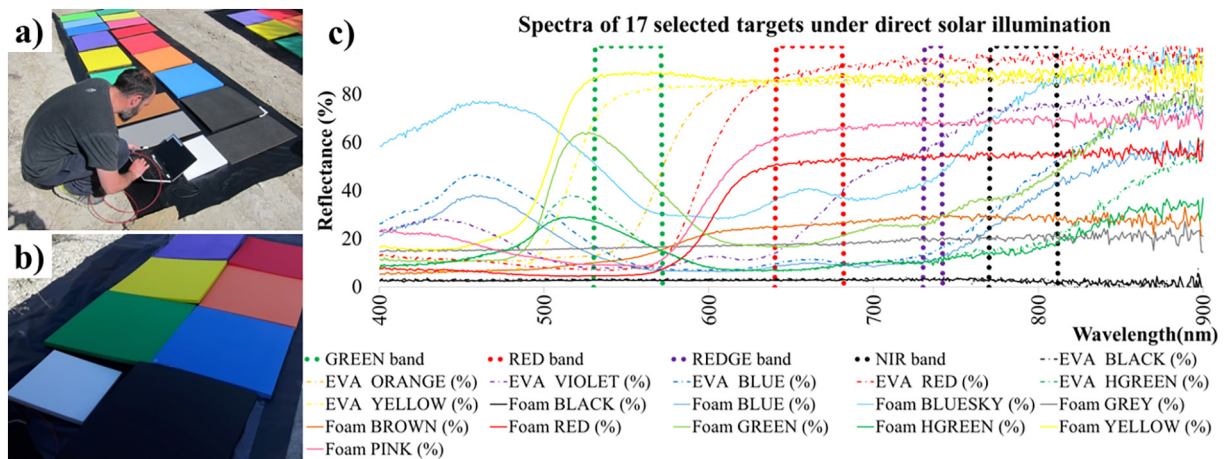


**Fig. 3.** Field spectroradiometric materials: (a) Field spectroradiometric measurements on targets (b) testing shadow effects (c) spectral signatures of targets, overlapped to Sequoia sensor bandwidth. The “foam” and the “EVA” panels differed in the size and, as seen in the spectral signature, in the color.

from those pixels also illuminated by direct Sun irradiance (non-shadowed pixels) to recover information from as much shadowed pixels as possible (Movia et al., 2016). In our approach, the detailed shadow detection was obtained combining empirical and physical methods (Adeline et al., 2013). In order to limit the possible histogram commissions within the geometrically candidate pixels, the joint conditions for selecting shadowed pixels was: i) under the histogram threshold of the first quartile in the intensity image, in the REG band and in the NIR band; ii) under the shadow of the Digital Cast Shadow Model (DCSM) or Digital Illumination Model (DIM) [self-shadows]. Once masked, the reduction was achieved with the invariant color model method (Adeline et al., 2013) taking advantage of radiometric values taken in pairs of targets located in shadowed and non-shadowed conditions simultaneously. Non-shadowed pixels and de-shadowed pixels were tagged and, finally, a 5 pixels  $\times$  5 pixels mean filter was applied in the boundary belt of de-shadowed areas to smooth the transition (cf. Fig. S7 in Supplementary materials). Afterwards, at-sensor drone data obtained with DLS was radiometrically corrected by applying the empirical line technique supported in field spectroscopy measurements, so as to improve the fitting to target references and correcting possible biases.

When radiometrically corrected, imagery was used for calculating spectral variables to statistically discriminate land covers at pixel resolution. A large quantity of spectral indices using VNIR information are related in the specialized literature, which focused on detecting vegetation (Xue and Su, 2017) and soil (Viscarra Rossel et al., 2016) features. In order to distinguish and quantify the area occupied by mine spoil outcrops from replaced topsoil (technosol) and the considered vegetation strata (grassland, shrubland and tree cover), multiple referenced indices were tested according to the availability of UAS sensor bands. Calculating the correlation matrix between all the tested indices and the spectral bands showed that indices with less redundant information included:

- i) Soil Adjusted Vegetation Index (SAVI) (Huete, 1988) [1] and Modified Soil Adjusted Vegetation Index 2 (MSAVI2) (Richardson and Weigand, 1977) [2], which minimize the effects of the soil background in the vegetation detection, and is widely used in soil erosion, drought and desertification analyses
  - [1]  $SAVI = (NIR - RED) \cdot 1.5 / (NIR + RED + 0.5)$
  - [2]  $MSAVI2 = 0.5 [2 NIR + 1 - \sqrt{(2 NIR + 1)^2 - 8 (NIR - RED)}]$
- ii) Normalized Difference Water Index 1 (NDWI1) (McFeeters, 1996) [3] which was designed to delimit water bodies. However, in the study area context, it enhances the detection of vegetation and soil moisture
  - [3]  $NDWI1 = (GRE - NIR) / (GRE + NIR)$
- iii) Normalized Difference Vegetation Index (NDVI) (Rouse et al., 1974) [4], which is the most used index to discriminate vegetation and monitor its evolution in multi-temporal analysis
  - [4]  $NDVI = (NIR - RED) / (NIR + RED)$ .

Soil and vegetation structural features were important inputs to describe the categories we aimed to map. Thus Digital Terrain Models (DTM) provided information that was not in the spectral bands and indices. Note that DTM are digital models that represent any variable, a DEM is a DTM where the variable is the terrain elevation, and a DSM is a DTM where the variable is the surface elevation (including vegetation, buildings, etc.). To this end, the DSM was the base for calculating the DIM and the DCSM used in the shadow reduction process, while the DEM was the base to calculate the Digital Slope Model and the

Digital Aspect Model used in the terrain morphology characterization and is capable of describing water runoff flows. A very valuable product is the height difference between the DSM and the DEM, which result in providing structural information ranging from the bare soil ( $\sim 0$  m of difference) up to the tree formations ( $>2$  m of difference).

### 3.3. Classification methods and accuracy evaluation

The automatic land cover classification was carried out using k-Nearest Neighbor (kNN) classification algorithm (Cover and Hart, 1967) implemented as a parallelized 64-bit version in the MiraMon software. kNN is particularly robust when different spectral responses are associated to a unique informational class (Vidal-Macua et al., 2017).

Ground-truth plots with a known land cover played a key role at this step. Delimited areas were digitized over the orthophotomap, whereby and half of them were used to train the classifiers (Training Areas, TA) and the other half was set aside to validate the thematic accuracy (Validation Areas, VA) (Fig. 4).

Six land cover categories in the legend of thematic areas were considered:

**Mine wastes:** Outcrops of bare mineral substrates, very poor in organic matter ( $<0.5\%$ ), and without vegetation, formerly not restored soil (mine spoils dump). This category is well characterized spectrally in the restored area with a  $<1\%$  standard deviation in in-situ measurements (Fig. 5).

**Topsoil:** Bare soil with any organic matter content ( $>0.5\%$ ) but without vegetation, replaced former soil coming from restoration activities (technosol). This category was well characterized spectrally in the restored area although a  $2\%$  standard deviation is observed throughout the measurements (Fig. 5).

**Tree cover:** Tree plant formations, typically forested zones of the latest stages in restored areas. Not only spectral features characterized this category, but structural information was used to consider that all vegetation pixels with a height AGL over 2 m corresponded to trees.

**Shrublands:** Plant formations of up to 2 m AGL, mainly bushes corresponding to medium successional stages. Several species and formations were included in this category, which also featured a wide spectral signature variety (Fig. 5).

**Grasslands:** Herbaceous plant formations with heights of up to 1 m, mainly consisting of grasses and forbs species that correspond to early successional stages in restored areas. Several grassland formations were included in this category, which featured a wide spectral signature variety (Fig. 5).

**Remaining shadows:** Shadows not corrected in the shadow reduction process can be considered as missing data. This category is scene-dependent (terrain morphology, solar zenith angle ( $\theta$ ) and solar azimuth angle ( $\phi$ )).

## 4. Results

UAS-acquired spectral information in green, red, red-edge and near-infrared wavelength regions resulted in generating orthophotomaps of 9 cm pixel size that clearly showed mine wastes, topsoil, and vegetation structures. Locations that were inaccessible to technicians could also be observed and registered. A systematic multispectral measurement was done over the entire area of interest, complementing the traditional transecting operations.

Radiometric correction resulted in a good fitting to ground-truth radiometric measurements. Although the coefficient of determination between field data and at-sensor (Sequoia) reflectance data was over 0.9 in all bands, bias and gain were not good enough for highly accurate

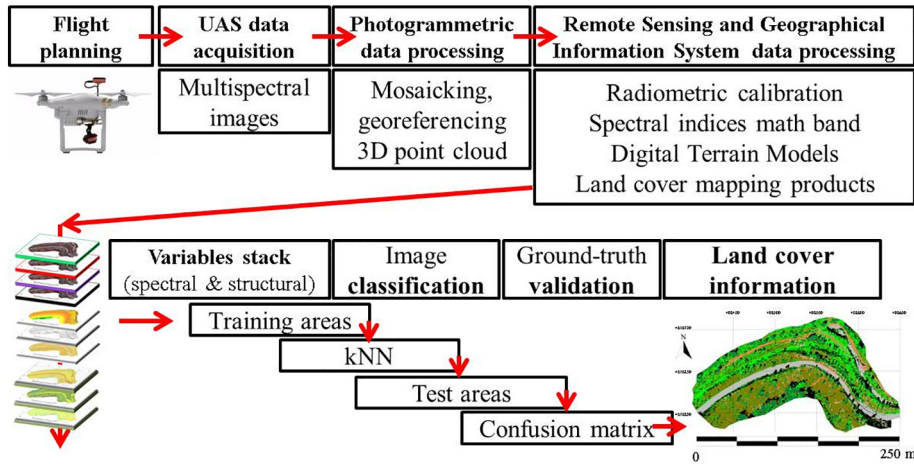


Fig. 4. General workflow for land cover mapping from UAS data using the kNN classifier.

applications. Establishing synergy between the conventional field spectroscopy measurements and novel UAS sensors, we finally applied the empirical line correction to at-sensor (DLS) reflectance values to fit the image data to in-situ observed values in the seven targets located in direct irradiance illumination conditions. However, we previously tested the accuracy of the results by performing the empirical line with three spectrally representative targets, including dark and bright ones, and evaluating the results with the remaining four. The obtained bias and gain clearly provided a better fitting to ground truth than fitting using the at-sensor Sequoia reflectance data. Once this was clarified, and given that the bias and gain values obtained using three or seven references provided similar model results, we finally applied the empirical line correction using all targets (seven) in order to minimize any error and obtain the more robust model. On the other hand, shadow reduction facilitated the process of classifying previously shadowed pixels, although the method was not perfect and some undetected shadows remained (Fig. 6).

Spectral information was combined to generate additional information and detect vegetation and soil properties (i.e. vegetation activity (NDVI), moisture content (NDWI1)). By visualizing false color combinations of drone images it was intuitive to find the presence of vegetation due to the high response of active vegetation in the NIR band. By mapping spectral indices, we could focus on the spatial distribution of the vegetation presence and activity (NDVI), the moisture content (NDWI1) and the soil effects on vegetated areas (SAVI and MSAVI2), which altogether facilitated in the process of quantifying vegetated areas and non-vegetated areas at 9 cm × 9 cm pixels (Fig. 7).

Additionally, structural information about the terrain morphology was constructed from the DEM and allowed simple topographic

products as contour line vector maps, which, in combination with official topographic maps could complement the terrain morphology monitoring. Combining the information on sun position and the DSM, important landscape and ecological information was retrieved, as the vegetation projected shadows and sun illumination rates. Moreover, the differential map between the DSM and the DEM provided relevant information about the relative heights of structures, and thus, the vegetation height AGL. Firstly, in the classification step, the layer of the differential map between DSM and DEM (in combination with the spectral information layers) was used to statistically contribute to distinguishing high vegetation from low vegetation; in this respect it is important to note that a pixel with a spectral response different to vegetation can have a relative height but is not classified as vegetation. Secondly, in the interpretation of the results step, those pixels classified as vegetation can be crossed with the differential map between DSM and DEM to determine the vegetation height (Fig. 8).

Finally, selected digital information was used to generate a stack of nine statistical variables (spectral and structural) to characterize each land cover. Four variables represented the spectral bands of the Parrot Sequoia (GRE, RED, REG and NIR radiometrically corrected), three variables represented the vegetation indices (SAVI, NDWI1 and NDVI), one variable represented the intensity part of the color space transformation and the remaining variable represented the AGL difference between the DSM and the DEM.

A total of 60,402 pixels were used as Training Areas for the digital classification process, which were selected by photointerpretation on delimited plots visible in the drone image. The combination of training data, statistical remote sensing variables and the kNN classification method, produced a land cover map where the categories of interest

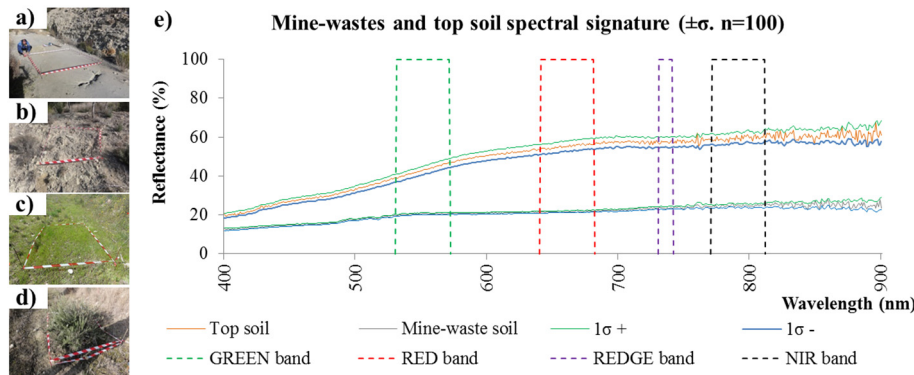
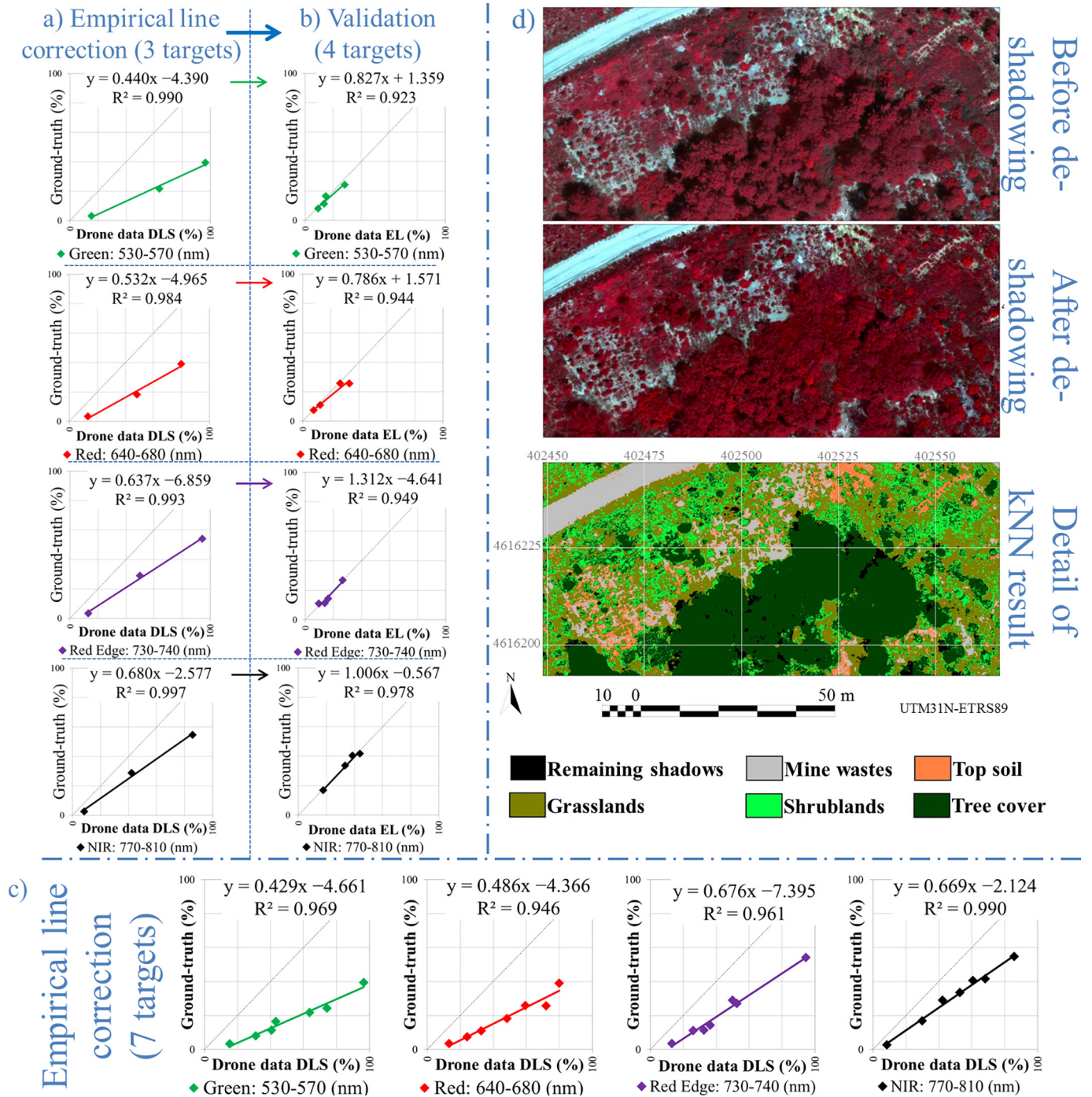


Fig. 5. Ground-truth data: Field plots of (a) mine-wastes soil (b) replaced topsoil (c) grasslands (d) shrublands (e) mine wastes and topsoil spectral signatures.



**Fig. 6.** Radiometric correction of drone data. (a) Regression resulting from the empirical line radiometric correction using three reference targets, of the empirical line correction performed from (a) results. (b) Validation, using four independent targets, of the empirical line correction performed from (a) results. (c) Regression resulting from the empirical line correction using seven targets (regression finally used for the empirical line correction). (d) Detail of the shadow reduction result in imagery and land cover classification (cf. Fig. S7 in Supplementary materials for more details).

were identified, and therefore individually monitored. A total of 11,872 pixels were used as test areas to evaluate the thematic accuracy. The overall accuracy was 94.71% and the kappa index was 0.92. The confusion matrix showed a good accuracy when splitting mine wastes and topsoil (>97%), tree cover was mapped with good results (>96%), and most of the confusion was found between grass and shrub vegetation, due principally to the intrinsic structural and spectral diversity of these categories (cf. Table S6 in the Supplementary materials).

The thematic land cover mapping was principally useful for quantifying diverse plant covered area and its spatial distribution trend, which

was carried out by considering all the restoration stages together or at each individual stage scale (Table 1).

The land cover area occupied in each restoration zone was monitored not only in absolute units, but also comparing relative changes in the internal distribution of each stage. The analysis of the internal variation of land covers distribution was found as one of the most interesting results of the provided information. The study area presented different restoration stages and in all of them, the spatial particularities were mapped, which constitute a valuable product for environmental managers (Fig. 9).

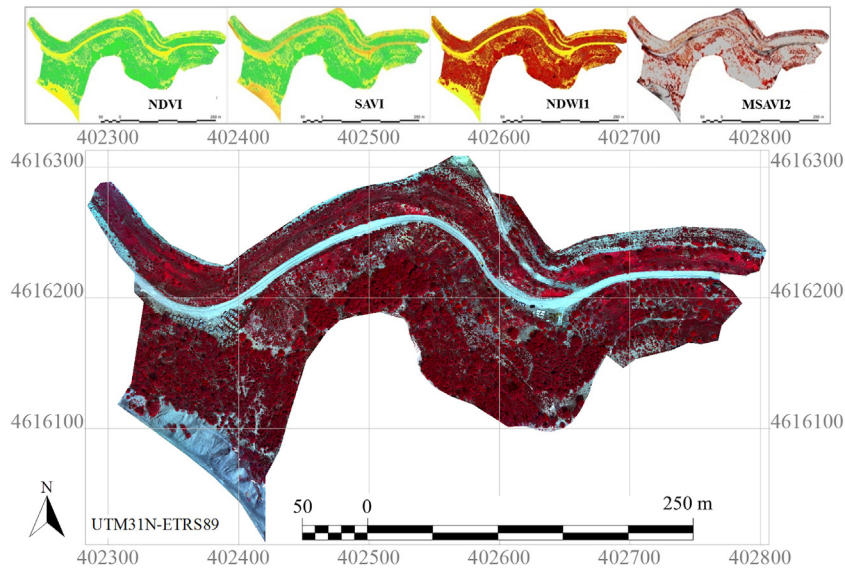


**Fig. 7.** Spectral information from UAS data: Top: Vegetation indices calculated with the RS&GIS software. Bottom: False color orthophoto generated from near-infrared, red and green bands.

The mapping products obtained were fully integrated into the actual official cartography, which locally improves both the spatial resolution and the temporal resolution. Therefore, the visual inspection of restoration processes is greatly improved, as it provides crucial information in the event that a regularly updated official orthoimagery would not be feasible. If previous cartography is available, UAS products are useful in detecting anomalies in the restoration process, and thus make it possible to focus on zones where vegetation development remains low (Fig. 10).

## 5. Discussion

This medium-sizes opencast mine restoration (<10 ha) was easily covered by a low-weight rotary-wing UAS. Fast multispectral information acquired from the UAS sensor is particularly interesting due to the spatial resolution (9 cm) and coverage (64,386 m<sup>2</sup>), which makes it possible to provide a very detailed visual inspection of the entire restored area, thus making it a highly valuable tool for controlling and

monitoring restored mining areas. In addition to scientific interest, introducing UAS into the periodic inspections of mine restorations could be considered as an objective and effective solution for reducing disagreements between public administration and private companies, and at the same time, contributing to monitoring the sustainable development of extractive mining activities.

Validation issues regarding radiometric corrections were solved in synergy with in-situ spectroradiometric measurements, using inexpensive reference panels. In this study we used a large number of targets to test different spectral responses and for validation purposes. Nevertheless, a lower number of radiometric references can be used for this application (Richter and Schläpfer, 2016). Indeed, the empirical line regression using seven targets and using three targets is very similar (Fig. 6), but in this study we used seven references to perform a more robust regression. The use of the Parrot Sequoia DLS did not provide satisfactory reflectance values, as demonstrated in the regressions between image data and field spectroscopy data (Fig. 6). The coefficient of determination was good ( $R^2 > 0.9$  in all bands) but the bias was higher

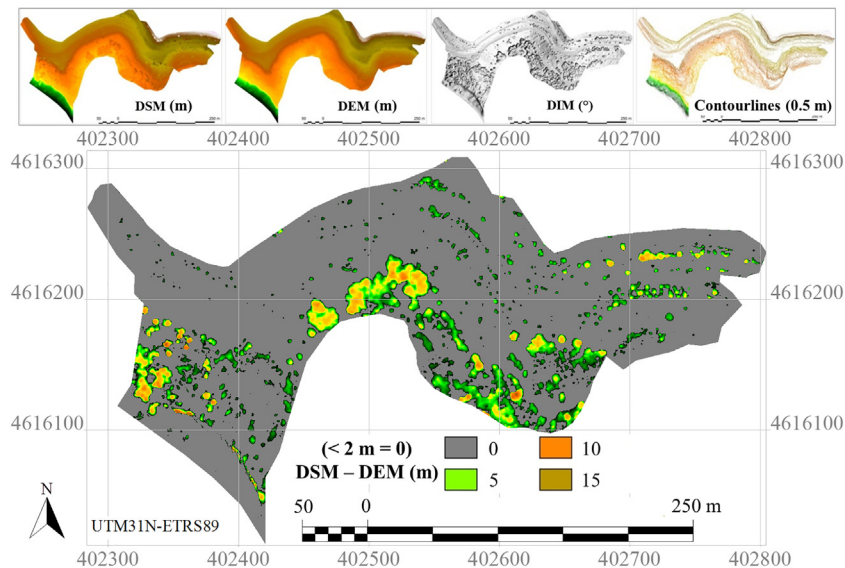


**Fig. 8.** Structural information from UAS data: Top: Digital Terrain Models accounting for vegetation, soil elevation, sun illumination and topographic contour line product. Bottom: Differential height between Digital Surface Model and Digital Elevation Model, representing vegetation height of over 2 m.

**Table 1**

Land cover area (m<sup>2</sup>) mapped by soil and vegetation typologies and restoration stages. Abbreviations: T<sub>0</sub> = 0–5 years, T<sub>1</sub> = 5–10 years, T<sub>2</sub> = 10–15 years, T<sub>3</sub> = 15–20 years, REF = Reference area, TRA = Transit Area, ROI = Region Of Interest.

Surface cover/stage	T <sub>0</sub>	T <sub>1</sub>	T <sub>2</sub>	T <sub>3</sub>	REF	TRA	Total
Mine wastes	829	2536	4426	3608	233	3601	15,233
Topsoil	28	240	241	603	130	51	1293
Tree cover	862	4700	6470	4932	5480	42	22,485
Shrubland	833	1895	2363	2977	1273	28	9370
Grassland	1802	3206	2962	6387	1039	265	15,661
Remaining shadows	10	51	175	54	51	4	345
Total ROI	4364	12,627	16,638	18,561	8206	3990	64,386

than 4% in visible bands and reached 7% in the red-edge band. These biases have been corrected using the empirical line correction by fitting the image to the reflectance of reference targets (Padró et al., 2018). Nevertheless, previous works that used more accurate DLS instruments have demonstrated that the use of upwards looking irradiance sensors is a good system for converting images to at-sensor reflectance (Hakala et al., 2018; Markelin et al., 2018), but the challenge in the aforementioned method is ensuring that the upwards looking sensor are consistently horizontally leveled. Shadow reduction allowed the recovering of information from pixels that would be lost in the land cover mapping, although a relatively few number of pixels remained classified as shadows due to conservative masking decisions, as pointed out in previous studies (Movia et al., 2016; Adeline et al., 2013).

Band calculation using near infrared and visible information facilitates the quantification of vegetation activity in intensity maps, which point out areas with high vegetation development and areas with vegetation cover deficits. Using photogrammetric DSM and DEM provided the essential basis creating derived terrain models that contributed in obtaining valuable information by computing the sun illumination received in every pixel, the detailed terrain slope, or the vegetation height. It is worthy noting that spatial resolution of 9 cm is a fine systematic landscape sampling, which is enough to establish vegetation height classes reflecting the dynamics of the vegetation cover from the initial phases to the more advanced stages of the restoration. Airborne lidar data could typically offer spatial resolutions and samplings below 1 m, and rarely below 10 cm at low-cost. However, lidar sensors are currently being tested in combination with UAS platforms that could allow ultra-high spatial sampling. Perhaps in the future, the presented protocol could be complemented with lidar sensors. However, for many, the high expense of using and maintaining lidar sensors can prove ultimately non-cost effective (Manfreda et al., 2018). As a more viable alternative, photogrammetric solutions, such as those presented in this paper, offer more than reasonable answers to opencast mine restoration monitoring. Although the use of low-cost UAS imagery for monitoring purposes is plenty operative in developed countries, we point to developing countries, where often there are higher economically constrains. In this land cover degradation and restoration study, we found a solution that can effectively contribute towards integrating scientific methods and technologies, while working towards

economically robust transitions in environmental management in accordance with the Sustainable Development Goals (United Nations, 2018).

The categorical treatment of land surfaces led to the quantification of the area covered by the different soil and vegetation types: not only within the overall restoration range, but also specifically within the different restoration stages. Detecting and distinguishing topsoil and mine waste cover was carried out and yielded good results. This is important when considering that topsoil and mine waste cover pose real concerns for identifying and interpreting restoration failures and risks (Espigares et al., 2011). Indeed, on the one hand, bare soil cover could be an indicator of sowings and planting failures, and/or of poor soil quality, which increase the risk of erosion (Van der Knijff et al., 2000; Espigares et al., 2011). On the other hand, mine waste dumping or mine waste used as soil substitute without a proper organic and/or mineral amendment, heavily limits vegetation establishment and encroachment, supposing an unacceptable situation in mine restoration (Ram et al., 2006; Jordán et al., 2008). Therefore, an expedient and precise quantification of these types of land cover is a useful tool for estimating erosion risks or soil quality limitations. Regarding monitoring vegetation and soil at stages, grasslands were the dominant cover in T<sub>0</sub> but some areas covered by mine wastes were still detected. Therefore, corrective measures are still imperative for improving vegetation encroachment (Jordán et al., 2008). In the restored areas from five and ten years ago (T<sub>1</sub>) tree cover was relatively dominant in the landscape despite the same proportion of mine waste cover was detected. Restored areas from 10 and 15 years ago (T<sub>2</sub>) occupied the most extensive tree cover area of the four restoration scenarios considered, but also mine waste outcrops were the second land cover in this stage, which could be attributed to failing restoration processes in problematic areas (steeped slopes, slope > 90%). The late stage restoration scenario (T<sub>3</sub>), in which restoration measures were carried out >15 years ago, showed a land cover distribution far away from the reference landscape (REF) and the more recent stage considered, and thus demonstrating the need of revising the classical methodologies used for the restoration in this area. A plausible explanation of this result can be attributed to less exigent need for restoration regulations 20 years ago, whereby the usual practice at the time was the direct afforestation over the mine wastes with Aleppo pine (*P. halepensis*), without soil replacement, or over a very unfertile substrate.

A fixed-wing platform could be more suitable for much more extensive restorations and perhaps further improvements could be achieved using multispectral sensors with more bands (e.g. MicaSense RedEdge) or hyperspectral sensors with narrower bands to enhance the spectral information. Regarding image geometry, low-cost single-frequency GPS receivers do not allow direct georeferencing. As such, geometric accuracy relies on the accuracy of delimitation stacks used as GCPs, which mining companies are required to maintain by law, as well as the technician's skill to locate them in the imagery. A heavier multicopter typically offers more stability, while a fixed-wing platform typically offers much more autonomy and coverage, and a double-frequency carrier-phase GNSS provides much more direct georeferencing accuracy, and a lidar sensor could provide structural information (Listopad et al., 2015), but this material is much more expensive. Ultimately, our goal was to design a protocol that is low-cost and capable of offering acceptable results. The material is useful in different campaigns and costs altogether under 6000 €, which included the platform, the UAS sensor, the field spectroradiometer and the radiometric reference targets.

## 6. Conclusions

Monitoring opencast mining restoration with UAS imagery has been proven operational and useful, as it provides expedient and accurate spatial and thematic information. Resulting products can systematically and recurrently sample the restoration area of interest at sub-decimeter pixel size, which improves airborne imagery spatial resolution and allows monitoring in inaccessible, restricted or dangerous areas. In addition to the intrinsic

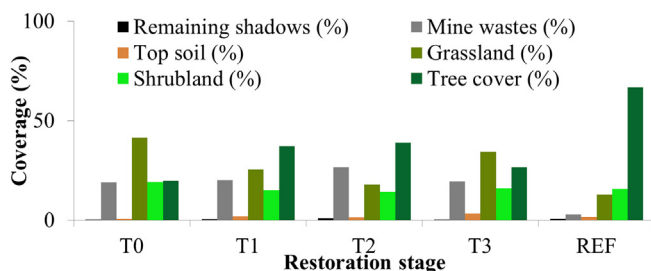
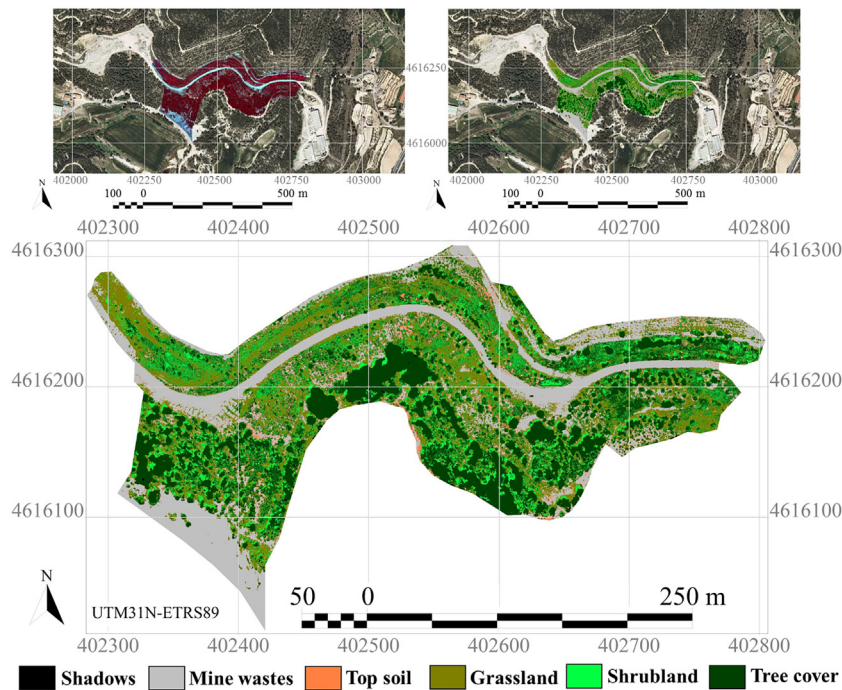


Fig. 9. Land cover relative distribution within each restoration stage.



**Fig. 10.** Top: False color orthophotomap and land cover classification result integrated with official cartography. Bottom: Land cover classification of the study area.

interest of the imagery for visual inspections, photogrammetric and RS&GIS software treatment provided additional spatial information about vegetation development and restoration failure or success, plant cover and height, mine waste dumping, bare soil cover, and geomorphic terrain features.

With the relatively low-cost material used in this study i.e. low-weight platform, multispectral sensor, low-cost radiometric reference panels and field spectroradiometer, it is possible to generate rigorous cartographical documentation as orthophotomaps, Digital Elevation Models, Digital Surface Models, vegetation indices and thematic land cover maps fully integrated to previous cartography and official databases. The inclusion of new unmanned aerial technologies gives us a glimpse of new horizons for monitoring restoration with inexpensive materials and intensive samplings.

Not only did automatic land cover mapping allow us to dispense with the manual photointerpretation, it also provided accuracies of over 94%, although individual focusing on problematic areas could also be improved manually, if needed. The overall workflow was highly automatized with batch processes. Nevertheless, it is convenient for the specialized technician to verify the correct execution and help in important decisions, such as digitizing of the training and testing areas. Moreover, compared to what would have been carried out in a conventional inspection of the restored areas, the fieldwork time in our case study was reduced considerably, which altogether included geometric stacks maintenance, field spectroradiometric measurements, and UAS flight. To summarize, the time used for obtaining ground-truth data and the UAS flight, 2 h is sufficient for inspecting a restored area of 10 ha, while data processing can be fully done by one person in two working days. It is worth noting that while UAS can help and support the monitoring of restoration activities, it should not by any means replace in-situ inspections or technician supervision.

In addition to the interest of monitoring older restorations with an unprecedented detail, current UAS remote sensing products will certainly become a valuable precedent for future opencast mine monitoring studies all around the world, as it provides improved time-series information. Considering the potential, the obtained results and the objective information produced, the proposed protocol can be a suitable tool for administrations, mining and consulting companies as well as for environmental scientists.

## Acknowledgments

This work was supported by the European Union as part of the ECOPOTENTIAL Project (H2020 641762-2 EC), by an Innovation grant from the Spanish Ministry of Science and Innovation (ACAPI, CGL2015-69888-P (MINECO/FEDER-ERDF, EU)), and by the Catalan Government (Department of Territory and Sustainability) under the project “Research and innovation in the monitoring and process of extractive activities restoration”. GRUMETS Research Group is partially supported by the Catalan Government under Grant (SGR2017-1690). Joan-Cristian Padró is a recipient of the FI-DGR scholarship grant (2016B\_00410). Xavier Pons is a recipient of the ICREA Academia Excellence in Research Grant (2016–2020).

## Author contributions

C.P. and V.C. conceived and designed the experiments. J.B., V.C. and C.P., performed the field data experiments. C.P. and V.C. analyzed the data. C.P., V.C. and X.P. wrote the paper. L.B., J.A. and X.P. supervised the paper and the overall experiments.

## Conflicts of interest

The authors declare that there are no conflicts of interest. The founding sponsors had no role in the design of the study; in the collection, analyses, or interpretation of data; in the writing of the manuscript, or in the decision to publish the results.

## Appendix A. Supplementary data

Supplementary data to this article can be found online at <https://doi.org/10.1016/j.scitotenv.2018.12.156>.

## References

- Aasen, H., Burkart, A., Bolten, A., Bareth, G., 2015. Generating 3D hyperspectral information with lightweight UAV snapshot cameras for vegetation monitoring: from camera calibration to quality assurance. *ISPRS J. Photogramm. Remote Sens.* 108, 245–259. <https://doi.org/10.1016/j.isprsjprs.2015.08.002>.

- Abdollahnejad, A., Panagiotidis, D., Surový, P., Ulbrichová, I., 2018. UAV capability to detect and interpret solar radiation as a potential replacement method to hemispherical photography. *J. Remote Sens.* 10 (3), 423–440. <https://doi.org/10.3390/rs10030423>.
- Adeline, K.R.M., Chen, M., Briottet, X., Pang, S.K., Paparoditis, N., 2013. Shadow detection in very high spatial resolution aerial images: a comparative study. *ISPRS J. Photogramm. Remote Sens.* 80, 21–38. <https://doi.org/10.1016/j.isprsjprs.2013.02.003>.
- Agisoft LLC, 2018. PhotoScan user manual, professional edition, version 1.4. [http://www.agisoft.com/pdf/photoscan-pro\\_1.4\\_en.pdf](http://www.agisoft.com/pdf/photoscan-pro_1.4_en.pdf), Accessed date: 1 November 2018.
- Ahmed, O.S., Shemrock, A., Chabot, D., Dillon, C., Williams, G., Wasson, R., Franklin, S.E., 2017. Hierarchical land cover and vegetation classification using multispectral data acquired from an unmanned aerial vehicle. *Int. J. Remote Sens.* 38, 2037–2052. <https://doi.org/10.1080/101431161.2017.1294781>.
- ASPRS (American Society for Photogrammetry and Remote Sensing), 2014. ASPRS Positional Accuracy Standards for Digital Geospatial Data. Edition 1, version 1.0.0. URL: [http://www.asprs.org/a/society/divisions/pad/Accuracy/ASPRS\\_Positional\\_Accuracy\\_Standards\\_for\\_Digital\\_Geospatial\\_Data\\_Edition1\\_V1\\_FinalDraftForPublication.docx](http://www.asprs.org/a/society/divisions/pad/Accuracy/ASPRS_Positional_Accuracy_Standards_for_Digital_Geospatial_Data_Edition1_V1_FinalDraftForPublication.docx), Accessed date: 1 November 2018.
- Bonifazi, G., Cutaiia, L., Massacci, P., Roselli, I., 2003. Monitoring of abandoned quarries by remote sensing and in situ surveying. *Ecol. Model.* 170, 213–218. [https://doi.org/10.1016/S0304-3800\(03\)00228-X](https://doi.org/10.1016/S0304-3800(03)00228-X).
- Bradshaw, A., 1997. Restoration of mined lands - using natural processes. *Ecol. Eng.* 8, 255–269. [https://doi.org/10.1016/S0925-8574\(97\)00022-0](https://doi.org/10.1016/S0925-8574(97)00022-0).
- Capolupo, A., Pindozi, S., Okello, C., Fiorentino, N., Boccia, L., 2015. Photogrammetry for environmental monitoring: the use of drones and hydrological models for detection of soil contaminated by copper. *Sci. Total Environ.* 514, 298–306. <https://doi.org/10.1016/j.scitotenv.2015.01.109>.
- Chavez Jr., P.S., 1988. An improved dark-object subtraction technique for atmospheric scattering correction of multispectral data. *Remote Sens. Environ.* 24, 459–479. [https://doi.org/10.1016/0034-4257\(88\)90019-3](https://doi.org/10.1016/0034-4257(88)90019-3).
- Chen, J., Li, K., Chang, K.-J., Sofia, G., Tarolli, P., 2015. Open-pit mining geomorphic feature characterization. *Int. J. Appl. Earth Obs. Geoinf.* 42, 76–86. <https://doi.org/10.1016/j.jag.2015.05.001>.
- Cover, T., Hart, P., 1967. Nearest neighbor pattern classification. *IEEE Trans. Inf. Theory* 13 (1), 21–27. <https://doi.org/10.1109/TIT.1967.1053964>.
- Díaz-Varela, R.A., De La Rosa, R., León, L., Zarco-Tejada, P.J., 2015. High-resolution airborne UAV imagery to assess olive tree crown parameters using 3D photo reconstruction: application in breeding trials. *Remote Sens.* 7 (4), 4213–4232. <https://doi.org/10.3390/rs70404213>.
- DITR (Department of Industry, Tourism and Resources), 2016. Mine Rehabilitation. Australian Government 0-642-72481-4, p. 77 URL: <https://archive.industry.gov.au/resource/Documents/LPSDP/LPSDP-MineRehabilitationHandbook.pdf>, Accessed date: 1 November 2018.
- DJI, 2018. Phantom 3 Professional. URL: <https://www.dji.com/es/phantom-3-pro/info>, Accessed date: 1 November 2018.
- Drake, J.A., Greene, R.S.B., Macdonald, B.C.T., Field, J.B., Pearson, G.L., 2010. A review of landscape rehabilitation in ecosystem engineering for mine closure. In: Fourie, A., Tibett, M., Wiertz, J., Perth, W.A. (Eds.), *Proceedings of International Conference on Mine Closure*. Australian Center for Geomechanics, pp. 241–249.
- Eisenbeiss, H., Zhang, L., 2006. Comparison of DSMs generated from mini UAV imagery and terrestrial laser scanner in a cultural heritage application. *ISPRS Commission V Symposium 'Image Engineering and Vision Metrology'*, IAPRS Volume XXXVI, Part 5, Dresden 25–27 Sep. 2006, pp. 90–96.
- Elmqvist, T., Folke, C., Nystrom, M., Peterson, G., Bengtsson, J., Walker, B., Norberg, J., 2003. Response diversity, ecosystem change and resilience. *Front. Ecol. Environ.* 1, 488–494. [https://doi.org/10.1890/1540-9295\(2003\)001\[0488:RDECAR\]2.0.CO;2](https://doi.org/10.1890/1540-9295(2003)001[0488:RDECAR]2.0.CO;2).
- ESA (European Space Agency), 2015. Sentinel-2A user handbook. Rev. 2. URL: [https://sentinel2.copernicus.eu/web/sentinel/user-guides/document-library/-/asset\\_publisher/xslst4309D5h/content/sentinel-2-user-handbook](https://sentinel2.copernicus.eu/web/sentinel/user-guides/document-library/-/asset_publisher/xslst4309D5h/content/sentinel-2-user-handbook), Accessed date: 1 November 2018.
- Espigares, T., Moreno-de las Heras, M., Nicolau, J.M., 2011. Performance of vegetation in reclaimed slopes affected by soil erosion. *Restor. Ecol.* 19, 35–44. <https://doi.org/10.1111/j.1526-100X.2009.00546.x>.
- Fernández-Guisuraga, J.M., Sanz-Ablanedo, E., Suárez-Seoane, S., Calvo, L., 2018. Using unmanned aerial vehicles in postfire vegetation survey campaigns through large and heterogeneous areas: opportunities and challenges. *Sensors* 18 (2), 586. <https://doi.org/10.3390/s18020586>.
- GENCAT (Generalitat de Catalunya), 2018. Orígens i evolució de la mineria (Origins and evolution of mining). Available online: [http://www.genocat.cat/icaen/recorregutenergia/unitat14/bloc3\\_unitat14\\_pag13.html](http://www.genocat.cat/icaen/recorregutenergia/unitat14/bloc3_unitat14_pag13.html), Accessed date: 1 November 2018.
- Granshaw, S.I., Fraser, C.S., 2015. Editorial: computer vision and photogrammetry: interaction or introspection? *Photogramm. Rec.* 30, 3–7. <https://doi.org/10.1111/phor.12092>.
- Hakala, T., Markelin, L., Honkavaara, E., Scott, B., Theocharous, T., Nevalainen, O., Näsi, R., Suomalainen, J., Viljanen, N., Greenwell, C., Fox, N., 2018. Direct reflectance measurements from drones: sensor absolute radiometric calibration and system tests for forest reflectance characterization. *Sensors* 18, 1417. <https://doi.org/10.3390/s18051417>.
- Hartley, R., Zisserman, A., 2003. *Multiple View Geometry in Computer Vision*. Cambridge University Press 0521540518.
- Honkavaara, E., Kaivosoja, J., Mäkynen, J., Pellikka, I., Pesonen, L., Saari, H., Salo, H., Hakala, T., Markelin, L., Rosnell, T., 2012. Hyperspectral reflectance signatures and point clouds for precision agriculture by light weight UAV imaging system. *ISPRS Annals of Photogrammetry, Remote Sensing and Spatial Information Sciences* vol. 1-7, pp. 353–358. <https://doi.org/10.5194/isprannals-1-7-353-2012>.
- Huete, A.R., 1988. A soil-adjusted vegetation index (SAVI). *Remote Sens. Environ.* 25 (3), 259–309. [https://doi.org/10.1016/0034-4257\(88\)90106-X](https://doi.org/10.1016/0034-4257(88)90106-X).
- Hüttel, R.F., Weber, E., 2001. Forest ecosystem development in post-mining landscapes: a case study of the Lusatian lignite district. *Naturwissenschaften* 88 (8), 322–329. <https://doi.org/10.1007/s001140100241>.
- ICAO (International Civil Aviation Organization), 2011. "Unmanned Aircraft Systems (UAS)". CIR328 AN/190.
- ICGC (Institut Cartogràfic i Geològic de Catalunya), 2018a. Full 274–99 de l'Ortofoto de Catalunya 1:2500 (OF–25C) (1:2500 Catalonia orthophoto Tile 274–99). URL: <http://www.icc.cat/vissir3/>, Accessed date: 1 November 2018.
- ICGC (Institut Cartogràfic i Geològic de Catalunya), 2018b. VISSIR, Visor de avançat de geoinformació de Catalunya (VISSIR, Advanced geoinformation viewer of Catalonia). URL: <http://www.icc.cat/vissir3/>, Accessed date: 1 November 2018.
- Iqbal, F., Lucieer, A., Barry, K., 2018. Simplified radiometric calibration for UAS-mounted multispectral sensor. *Eur. J. Remote Sens.* 51 (1), 301–313. <https://doi.org/10.1080/22797254.2018.1432293>.
- Jhan, J.P., Rau, J.Y., Haala, N., Cramer, M., 2017. Investigation of parallax issues for multi-lens multispectral camera band co-registration. *Int. Arch. Photogramm. Remote Sens. Spat. Inf. Sci. XLII-2/W6*, 157–163. <https://doi.org/10.5194/isprs-archives-XLII-2-W6-157-2017>.
- Jordán, M.M., Pina, S., García-Orenes, F., Almendro-Candel, M.B., García-Sánchez, E., 2008. Environmental risk evaluation of the use of mine spoils and treated sewage sludge in the ecological restoration of limestone quarries. *Environ. Geol.* 55, 453–462. <https://doi.org/10.1007/s00254-007-0991-4>.
- Kaufman, Y.J., Sendra, C., 1988. Algorithm for automatic atmospheric corrections to visible and near-IR satellite imagery. *Int. J. Remote Sens.* 9, 1357–1381. <https://doi.org/10.1080/01431168808954942>.
- Korjus, H., Laarmann, D., Sims, A., Paluots, T., Kangur, A., 2014. Assessment of novel forest ecosystems on post-mining restoration site in Aidu, Estonia. In: Polgár, A., Bazsó, T., Nagy, G., Gálos, B. (Eds.), *Local and Regional Challenges of Climate Change Adaptation and Green Technologies*. University of West Hungary Press, Sopron, pp. 35–44. <https://doi.org/10.13140/2.1.4557.6640>.
- Kraaijenbrink, P., Meijer, S.W., Shea, J.M., Pellicciotti, F., De Jong, S.M., Immerzeel, W.W., 2016. Seasonal surface velocities of a Himalayan glacier derived by automated correlation of unmanned aerial vehicle imagery. *Ann. Glaciol.* 57 (71), 103–113. <https://doi.org/10.3189/2016AoG71A072>.
- Listopad, C., Masters, R., Drake, J., Weishampel, J., Branquinho, C., 2015. Structural diversity indices based on airborne LiDAR as ecological indicators for managing highly dynamic landscapes. *Ecol. Indic.* 57, 268–279. <https://doi.org/10.1016/j.ecolind.2015.04.017>.
- Lucieer, A., Turner, D., King, D.H., Robinson, S.A., 2014. Using an Unmanned Aerial Vehicle (UAV) to capture micro-topography of Antarctic moss beds. *Int. J. Appl. Earth Obs. Geoinf.* 27, 53–62. <https://doi.org/10.1016/j.jag.2013.05.011>.
- Manfreda, S., McCabe, M., Miller, P., Lucas, R., Pajuelo Madrigal, V., Mallinis, G., Ben-Dor, E., Helman, D., Estes, L., Ciraolo, G., Müllerová, J., Tauro, F., de Lima, M.L., de Lima, J., Maltes, A., Francés, F., Caylor, K., Kohv, M., Perks, M., Tóth, B., 2018. On the use of Unmanned Aerial Systems for environmental monitoring. *Remote Sens.* 10, 641–669. <https://doi.org/10.3390/rs10040641>.
- Markelin, L., 2013. Radiometric Calibration, Validation and Correction of Multispectral Photogrammetric Imagery. pp. 1–86 URL: <https://aaltdoc.aalto.fi/bitstream/handle/123456789/10948/isbn9789517112956.pdf?sequence=1&isAllowed=y> (Doctoral dissertation for the degree of Doctor of Science in Technology, Aalto University School of Engineering, Espoo, Finland, September 2013).
- Markelin, L., Suomalainen, J., Hakala, T., Oliveira, R., Viljanen, N., Näsi, R., Scott, B., Theocharous, T., Greenwell, C., Fox, N., Honkavaara, E., 2018. Methodology for direct reflectance measurement from a drone: system description, radiometric calibration and latest results. *ISPRS - International Archives of the Photogrammetry, Remote Sensing and Spatial Information Sciences* vol. XLII-1, pp. 283–288. <https://doi.org/10.5194/isprs-archives-XLII-1-283-2018>.
- Mather, A.S., Needle, C.L., 1998. The forest transition: a theoretical basis. *Area* 30, 117–124. <https://doi.org/10.1111/j.1475-4762.1998.tb00055.x>.
- McFeeters, S.K., 1996. The use of the normalized difference water index (NDWI) in the delineation of open water features. *Int. J. Remote Sens.* 17, 1425–1432. <https://doi.org/10.1080/01431169608948714>.
- Meroni, M., Colombo, R., 2009. 3S: a novel program for field spectroscopy. *Comput. Geosci.* 35, 1491–1496. <https://doi.org/10.1016/j.cageo.2009.01.005> URL: <https://www.sciencedirect.com/science/article/pii/S0098300409000922>, Accessed date: 1 November 2018.
- Minerals Council of Australia, 2015. In: *Minerals Council of Australia* (Ed.), *Mine Rehabilitation in the Australian Minerals Industry*, p. 48 URL: [http://www.minerals.org.au/file\\_upload/files/reports/Mine\\_rehabilitation\\_in\\_the\\_Australian\\_minerals\\_industry\\_FINAL.pdf](http://www.minerals.org.au/file_upload/files/reports/Mine_rehabilitation_in_the_Australian_minerals_industry_FINAL.pdf), Accessed date: 1 November 2018.
- Movia, A., Beinat, A., Crosilla, F., 2016. Shadow detection and removal in RGB VHR images for land use unsupervised classification. *ISPRS J. Photogramm. Remote Sens.* 119, 485–495. <https://doi.org/10.1016/j.isprsjprs.2016.05.004>.
- NASA (National Aeronautics and Space Administration), 2018. Landsat Science. URL: <https://landsat.gsfc.nasa.gov/about/history/>, Accessed date: 1 November 2018.
- OceanOptics, 2006. USB200+ Data Sheet. OceanOptics, Dunedin, FL, p. 38 URL: <https://oceanoptics.com/wp-content/uploads/OEM-Data-Sheet-USB2000-.pdf>, Accessed date: 1 November 2018.
- Ockendon, N., Thomas, D., Cortina, J., Adams, W., Aykroyd, T., Barov, B., Boitani, L., Bonn, A., Branquinho, C., Brombacher, M., Burrell, C., Carver, S., Crick, H., Duguy, B., Everett, S., Fokkens, B., Fuller, R.J., Gibbons, D.W., Gokhleshvili, R., Sutherland, W., 2018. One hundred priority questions for landscape restoration in Europe. *Biol. Conserv.* 221. <https://doi.org/10.1016/j.biocon.2018.03.002>.

- Padró, J.-C., Badia, A., 2017. L'incendi de 1998 a la Catalunya Central. Anàlisi dels canvis en les cobertes del sòl (1956–2009) a diferents escales, d'incendi i de finca (The wildfire of 1998 in Central Catalonia. Analysis of land cover changes (1956–2009) at different scales: at the level of fire and property). *Treballs de la Societat Catalana de Geografia* 83, 79–108. <https://doi.org/10.2436/20.3002.01.125>.
- Padró, J.-C., Pons, X., Aragónés, D., Díaz-Delgado, R., García, D., Bustamante, J., Pesquer, L., Domingo-Marimon, C., González-Guerrero, O., Cristóbal, J., Doktor, D., Lange, M., 2017. Radiometric correction of simultaneously acquired Landsat-7/Landsat-8 and Sentinel-2A imagery using pseudo-invariant areas (PIA): contributing to the Landsat time series legacy. *Remote Sens.* 9 (12), 1319. <https://doi.org/10.3390/rs9121319>.
- Padró, J.-C., Muñoz, F.-J., Avila, L.-A., Pesquer, L., Pons, X., 2018. Radiometric correction of Landsat-8 and Sentinel-2A scenes using drone imagery in synergy with field spectroradiometry. *Remote Sens.* 10 (11), 1687. <https://doi.org/10.3390/rs10111687>.
- Padró, J.-C., Muñoz, F.-J., Planas, J., Pons, X., 2019. Comparison of four UAV georeferencing methods for environmental monitoring purposes focusing on the combined use with airborne and satellite remote sensing platforms. *Int. J. Appl. Earth Obs. Geoinf.* 75, 130–140. <https://doi.org/10.1016/j.jag.2018.10.018>.
- Pla, M., Duarte, A., Brotons, L., 2017. Potencial de las imágenes UAV como datos de verdad terreno para la clasificación de la severidad de quema de imágenes Landsat: aproximaciones a un producto útil para la gestión post incendio (Potential of UAV images as ground-truth data for the burning severity classification of Landsat imagery: approximations to a useful product for post-fire management). *Revista de teledetección* 49, 91–102. <https://doi.org/10.4995/raet.2017.7140>.
- Pons, X., 2016. MiraMon. Sistema d'Informació Geogràfica i software de Teledetecció. Versió 8.01b. Centre de Recerca Ecològica i Aplicacions Forestals, CREA, Bellaterra 84-931323-4-9 URL: <http://www.crea.uab.cat/miramon/>, Accessed date: 1 November 2018.
- Pons, X., Pesquer, L., Cristóbal, J., González-Guerrero, O., 2014. Automatic and improved radiometric correction of Landsat imagery using reference values from MODIS surface reflectance images. *Int. J. Appl. Earth Obs. Geoinf.* 33, 243–254. <https://doi.org/10.1016/j.jag.2014.06.002>.
- Pons, X., Moré, G., Cea, C., Serra, P., Mira, M., González, O., Zabala, A., Pérez, F., Tardá, A., Alamús, R., Palà, P., Lopez, A., 2015. A protocol for optimum usage of handheld spectroradiometers in airborne and satellite applications: the Ocean Optics USB2000+ case. *Proceedings of the 9th EARSeL SIG Imaging Spectroscopy Workshop, Luxembourg (Luxembourg)*, pp. 126–127 URL: [https://www.upf.edu/documents/3254890/0/program\\_short.pdf/bc40e341-f2a5-4b87-a89c-c8a84fe6fb8b](https://www.upf.edu/documents/3254890/0/program_short.pdf/bc40e341-f2a5-4b87-a89c-c8a84fe6fb8b), Accessed date: 1 November 2018.
- Poyatos, R., Latron, J., Llorens, P., 2003. Land use and land cover change after agricultural abandonment. *Mt. Res. Dev.* 23, 362–368. [https://doi.org/10.1659/0276-4741\(2003\)023\[0362:LJALCC\]2.0.CO;2](https://doi.org/10.1659/0276-4741(2003)023[0362:LJALCC]2.0.CO;2).
- Ram, L.C., Srivasta, N.K., Tripathi, R.C., Jha, S.K., Sinha, A.K., Singh, G., Manoharan, V., 2006. Management of mine spoils for crop productivity with lignite fly ash and biological amendments. *J. Environ. Manag.* 79, 173–187. <https://doi.org/10.1016/j.jenvman.2005.06.008>.
- Rehak, M., Skaloud, J., 2017. Time synchronization of consumer cameras on Micro Aerial Vehicles. *ISPRS J. Photogramm. Remote Sens.* 123, 114–123. <https://doi.org/10.1016/j.isprsjprs.2016.11.009>.
- Richardson, A.J., Weigand, C.L., 1977. Distinguishing vegetation from soil background information. *PE&RS* 43, 1541–1552 URL: [https://www.asprs.org/wp-content/uploads/pers/1977journal/dec/1977\\_dec\\_1541-1552.pdf](https://www.asprs.org/wp-content/uploads/pers/1977journal/dec/1977_dec_1541-1552.pdf), Accessed date: 1 November 2018.
- Richter, R., Schläpfer, D., 2016. Atmospheric/Topographic Correction for Satellite Imagery (ATCOR-2/3 User Guide, Version 9.0.2, March 2016). URL: [http://www.rese.ch/pdf/atcor3\\_manual.pdf](http://www.rese.ch/pdf/atcor3_manual.pdf), Accessed date: 1 November 2018.
- Rouse Jr., J.W., Haas, R., Schell, J., Deering, D., 1974. Monitoring vegetation systems in the Great Plains with ERTS. Third ERTS Symposium. NASA Special Publication 351, pp. 309–317 URL: <https://ntrs.nasa.gov/archive/nasa/casi.ntrs.nasa.gov/19740022614.pdf>, Accessed date: 1 November 2018.
- Rumpler, M., Daftry, S., Tscharf, A., Pretenthaler, R., Hoppe, C., Mayer, G., Bischof, H., 2014. Automated end-to-end workflow for precise and geo-accurate reconstructions using fiducial markers. *ISPRS Technical Commission III Symposium*, 5–7 September 2014, Zurich, Switzerland, pp. 135–142 <https://doi.org/10.5194/isprsannals-II-3-135-2014>.
- Sanders, A., 2017. Mapping the distribution of understory *Rhododendron ponticum* using low-tech multispectral UAV derived imagery. In: Díaz-Delgado, R., Lucas, R., Hurford, C. (Eds.), *The Roles of Remote Sensing in Nature Conservation. A Practical Guide and Case Studies*. Springer International Publishing AG 2017, Springer, Cham, Switzerland. ISBN: 978-3-319-64332-8, pp. 167–181.
- Schaepmann-Strub, G., Schaepmann, M.E., Painter, T.H., Dangel, S., Martonchik, J.V., 2006. Reflectance quantities in optical remote sensing – definitions and case studies. *Remote Sens. Environ.* 103, 27–42. <https://doi.org/10.1016/j.rse.2006.03.002>.
- Skaloud, J., Rehak, M., Licht, D., 2014. Mapping with MAV: experimental study on the contribution of absolute and relative aerial position control. *ISPRS - International Archives of the Photogrammetry, Remote Sensing and Spatial Information Sciences, Volume XL-3/W1*, 2014. EuroCOW 2014, the European Calibration and Orientation Workshop, 12–14 Feb. 2014, Castelldefels, Spain <https://doi.org/10.5194/isprsarchives-XL-3-W1-123-2014>.
- Thenkabail, P.S., 2015. *Land Resources Monitoring, Modeling, and Mapping With Remote Sensing*. CRC Press, Boca Raton, FL, USA 9781482217957.
- Turner, D., Lucieer, A., Malenovský, Z., King, D.H., Robinson, S.H., 2014. Spatial co-registration of ultra-high resolution visible, multispectral and thermal images acquired with a micro-UAV over Antarctic moss beds. *Remote Sens.* 6, 4003–4024. <https://doi.org/10.3390/rs6054003>.
- United Nations, 2018. Sustainable development goals. URL: <https://www.un.org/sustainabledevelopment/sustainable-development-goals/>, Accessed date: 1 November 2018.
- Van der Knijff, J.M., Jones, R.J.A., Montanarella, L., 2000. *Soil Erosion Risk Assessment in Europe*. European Soil Bureau, Joint Research Center, Ispra (34 pp.).
- Vermote, E., Justice, C., Claverie, M., Franch, B., 2016. Preliminary analysis of the performance of the Landsat8/OLI land surface reflectance product. *Remote Sens. Environ.* 185, 46–56. <https://doi.org/10.1016/j.rse.2016.04.008>.
- Vidal-Macua, J.J., Zabala, A., Ninyerola, M., Pons, X., 2017. Developing spatially and thematically detailed backdated maps for land cover studies. *Int. J. Digital Earth* 10 (2), 175–206. <https://doi.org/10.1080/17538947.2016.1213320>.
- Viscarra Rossel, R.A., Behrens, T., Ben-Dor, E., Brown, D.J., Dematté, J.A.M., Shepherd, K.D., Shi, Z., Stenberg, B., Stevens, A., Adamchuk, V., Aichi, H., Barthès, B.G., Bartholomeus, H.M., Bayer, A.D., Bernoux, M., Böttcher, K., Brodský, L., Du, C.W., Chappell, A., Fouad, Y., Genot, V., Gomez, C., Grunwald, S., Gubler, A., Guerrero, C., Hedley, C.B., Knadel, M., Morrá, H.J.M., Nocita, M., Ramirez-Lopez, L., Roudier, P., Rufasto Campos, E.M., Sanborn, P., Sellitto, V.M., Sudduth, K.A., Rawlins, B.G., Walter, C., Winowiecki, L.A., Hong, S.Y., Ji, W., 2016. A global spectral library to characterize the world's soil. *Earth Sci. Rev.* 155, 198–230. <https://doi.org/10.1016/j.earscirev.2016.01.012>.
- Xu, Z.-H., Wu, L.-X., Chen, S.-J., Wang, Z., 2015. Method of engineering volume monitoring and calculation for open-pit mine from UAV images. *J. Northeast. Univ. Nat. Sci.* 37 (1), 84–88. <https://doi.org/10.3969/j.issn.1005-3026.2016.01.018>.
- Xue, J., Su, B., 2017. Significant remote sensing vegetation indices: a review of developments and applications. *J. Sens.*, 1353691 <https://doi.org/10.1155/2017/1353691> (17).
- Yoo, H.-T., Lee, H., Chi, S., Hwang, B.-G., Kim, J., 2017. A preliminary study on disaster waste detection and volume estimation based on 3D spatial information. *Comput. Civ. Eng.*, 428–435 <https://doi.org/10.1061/9780784480823.051>.